This paper has been accepted for publication in the AEE journal. This is the version, which has not been fully edited and content may change prior to final publication.
Citation information: DOI 10.24425/aee.2026.3546

Dual-method 3D FEM-based determination of *d*-*q* inductances in axial-flux permanent magnet synchronous generator taking saturation, magnet material and air-gap effects into account

TOAN LUONG NGOC[1], THANH NGUYEN VU[2], DOAN DUC TUNG[1], VUONG DANG QUOC[2]*

[1]*Faculty of Engineering and Technology, Quy Nhon University, 170 An Duong Vuong Street, Quy Nhon Nam Ward, Gia Lai Province, Vietnam*
[2]*High Performance Electric Machines (HiPEMs), School of Electrical and Electronic Engineering Hanoi University of Science and Technology Hanoi, Vietnam*
*e-mail:{luongngoctoan/ddtung}@qnu.edu.vn, {*vuong.dangquoc/thanh.nguyenvu}@hust.edu.vn*

Abstract: This paper presents a method for determining the *d*- and *q*-axis inductances (L_d, L_q) of a 4 kW axial-flux permanent magnet synchronous generator (AFPMG) using combined 2D and 3D finite element method (FEM) simulation in Ansys Maxwell. The key contribution is a cross-validation framework employing two independent post-processing methods applied to the same FEM dataset: Method A, based on direct *dq* flux linkage extraction, and Method B, based on the phase inductance matrix (L_{abc}) combined with coordinate transformation. The *d*-*q* mathematical model, including voltage equations, flux linkages, and saturation effects, is first summarized. The complete 3D FEM simulation procedure is described, from geometry construction to inductance extraction, covering both static and transient analyses. The results demonstrate that both methods yield consistent inductance values, within a maximum deviation of approximately 7–8%. At rated current, $L_d \approx 6.8$ mH and $L_q \approx 6.4$ mH are obtained from 3D static simulation (Method A), confirming the reliability of the proposed simulation approach. The influence of magnetic saturation, magnet material, and air-gap length on L_d and L_q is also systematically investigated. The determined L_d and L_q values serve as essential parameters for field-oriented control (FOC) design of the AFPMG, enabling accurate torque and flux regulation.

Key words: 2D parametric study, 3D finite element method, axial-flux permanent magnet generator, *d*-*q* inductance, magnetic saturation

1. Introduction

Permanent magnet synchronous generators (PMSGs) of the axial flux permanent magnet (AFPM) type, such as the 4 kW machine studied in this paper, are attracting growing research interest owing to their advantages of high power density and flat, compact structure. In applications such as direct-drive wind turbines or small generators, the AFPMG allows designs with a large pole count and large disc diameter to achieve high torque at low speed. Accurate modeling of the AFPMG requires determination of the equivalent circuit parameters, the most important of which are the *d*-axis inductance (L_d) and *q*-axis inductance (L_q) [1–4, 8, 14].

The parameter set L_d, L_q plays a key role in the rotating-coordinate control model (field-oriented control - FOC) and in the calculation of the electromagnetic torque of a synchronous machine. However, due to magnetic saturation in the iron core and geometric asymmetry between the axes L_d, L_q may not be constant but depend on the operating point (armature current) as well as the rotor position angle, particularly in machines with iron-core teeth [6, 12]. With the AFPMG of the surface-mounted magnet type, it is theoretically geometrically symmetric, yielding $L_d \approx L_q$ [12]. However, under the effect of saturation in the teeth and yoke caused by the magnet field and load current, a certain degree of saliency still appears, causing L_d and L_q to differ and thereby generating reluctance torque. Therefore, an effective method is needed to accurately determine L_d and L_q under actual loaded conditions, as a basis for optimal design and control of the AFPMG [3, 5].

Many methods have been developed to calculate or measure L_d, L_q for electrical machines in general. Analytically, one can cite the reluctance-network model that separates magnetizing inductance from leakage inductance [7], the winding function and Fourier series method [9], or the co-energy method to derive the incremental inductance around an operating point [16]. Experimentally, the standstill frequency response (SSFR) method using small AC signals on each axis with the rotor locked is also a common approach for empirically deriving L_d, L_q [6]. Building on these analytical foundations, FEM-based approaches overcome the geometric and saturation limitations of analytical models and are therefore adopted in this work. Today, with advances in electromagnetic simulation technology, 2D/3D finite element method (FEM) simulation has proven useful in determining L_d, L_q parameters while accounting for saturation without requiring complex experimental tests. Especially for AFPMGs with complex 3D geometry, 3D FEM simulation enables accurate computation of the field distribution including edge effects such as tooth-tip leakage and end-winding effects [5, 7, 10, 12]. However, existing 3D FEM studies for the AFPMG typically employ only a single inductance extraction method, without cross-validation between approaches, and do not systematically investigate the combined effects of magnet material and air-gap length gaps that this paper addresses.

This paper presents a procedure to determine the inductances L_d, L_q of a 4 kW AFPMG using combined 2D and 3D finite element simulation in Ansys Maxwell software. While 2D simulation allows efficient parametric sweeps for studying the influence of magnet material and air-gap length, 3D simulation is required to capture end-winding effects and axial leakage flux inherent to the axial-flux topology. Two methods are applied in parallel: (A) based on *dq* flux linkage, and (B) based on the phase inductance matrix L_{abc} converted to the *dq* frame. In addition to the basic results from static 3D simulation, the paper systematically investigates influencing factors: magnetic saturation as a function of load current, the effect of including or excluding the magnet in the 2D model, the effect of magnet material (NdFeB and ferrite Y30), and the effect of air gap length. Results from 2D and 3D are cross-compared and verified through the electromagnetic torque from transient simulation [5, 12].

This paper has been accepted for publication in the AEE journal. This is the version, which has not been fully edited and content may change prior to final publication.
Citation information: DOI 10.24425/aee.2026.3546

2. Analytical background

2.1. The *dq* model of permanent magnet synchronous machines

A three-phase permanent magnet synchronous machine can be modeled in the stationary abc phase reference frame. The instantaneous voltage equation on each phase takes the form:

$$v_a = R\, i_a + \frac{\mathrm{d}\lambda_a}{\mathrm{d}t}, \quad v_b = R\, i_b + \frac{\mathrm{d}\lambda_b}{\mathrm{d}t}, \quad v_c = R\, i_c + \frac{\mathrm{d}\lambda_c}{\mathrm{d}t}, \tag{1}$$

where R is the phase resistance; λ_a, λ_b, and λ_c are the flux linkages of phases A, B, C respectively.

The flux linkage on each phase is expressed as:

$$\begin{aligned} \lambda_a &= L_{aa}(\theta)i_a + L_{ab}(\theta)i_b + L_{ac}(\theta)i_c + \lambda_{f,a}(\theta), \\ \lambda_b &= L_{ba}(\theta)i_a + L_{bb}(\theta)i_b + L_{bc}(\theta)i_c + \lambda_{f,b}(\theta), \\ \lambda_c &= L_{ca}(\theta)i_a + L_{cb}(\theta)i_b + L_{cc}(\theta)i_c + \lambda_{f,c}(\theta), \end{aligned} \tag{2}$$

where $L_{ij}(\theta)$ represents the self- and mutual inductances that vary periodically with rotor position θ, in contrast to the constant L_d and L_q values in the *d*-*q* frame; $\lambda_{f,a}$, $\lambda_{f,b}$, and $\lambda_{f,c}$ are the permanent magnet flux linkages with phases A, B, C.

To remove the rotor-position dependence of the phase model, the Clarke-Park transformation is applied, with the *d*-axis aligned with the rotor magnet axis; in the resulting rotating *dq* frame the steady-state quantities become DC.

Specifically, the voltage equations in the *dq* frame are given by:

$$\begin{cases} v_d = Ri_d + \frac{\mathrm{d}\psi_d}{\mathrm{d}t} - \omega_e\psi_q \\ v_q = Ri_q + \frac{\mathrm{d}\psi_q}{\mathrm{d}t} + \omega_e\psi_d \end{cases}, \tag{3}$$

where v_d represents the *d* and *q* axis stator voltages; i_d, i_q, ψ_d, and ψ_q are, respectively, the *d* and *q*-axis currents and flux linkages; R is the stator phase resistance.

Equation (3) holds for both steady-state and transient conditions and follows generator convention (current flowing out of the machine), the terms $\pm\omega_e\psi_{q,d}$ are the speed voltages induced by the rotating reference frame. The flux linkages in the *dq* frame for a PMSM can be modeled as:

$$\begin{cases} \psi_d = L_d i_d + \psi_f \\ \psi_q = L_q i_q \end{cases}, \tag{4}$$

where ψ_f is the permanent magnet flux linkage, entirely aligned with the *d*-axis for a surface-mounted PM (SPM) machine, and independent of armature current under unsaturated conditions. Note that Eq. (4) assumes no cross-axis saturation coupling, i.e., ψ_d depends only on i_d and ψ_q depends only on i_q. This simplification is justified for the operating range examined in this study, as discussed in Section 2.2. From the two expressions above, the definitions of inductance L_d (with i_q constant) and L_q (with i_d constant) can be derived [12].

This paper has been accepted for publication in the AEE journal. This is the version, which has not been fully edited and content may change prior to final publication.
Citation information: DOI 10.24425/aee.2026.3546

Differentiating Eq. (4) with respect to i_d, and noting that ψ_f is independent of i_d under unsaturated conditions, one obtains Eq. (5a). Similarly, differentiating with respect to i_q yields Eq. (5b)

$$L_d = \frac{\partial \psi_d}{\partial i_d}, \tag{5a}$$

$$L_q = \frac{\partial \psi_q}{\partial i_q}. \tag{5b}$$

Here L_d and L_q denote the incremental (differential) inductances at the operating point, representing the local slope of the flux linkage-current curve. Under linear unsaturated conditions, L_d, L_q are constants. When the magnetic core begins to saturate, the flux linkage-current relationship becomes nonlinear, and the inductance can then be characterized by the differential slope of the flux linkage-current curve at the operating point.

Figure 1 shows the corresponding *d-q* equivalent circuit (generator convention, zero-sequence flux neglected): each axis contains the stator resistance R_{ph}, the inductance L_d or L_q, and the speed-voltage sources $\omega_e L_q i_q$, $\omega_e L_d i_d$ and $\omega_e \lambda_m$, the last producing the constant generator back-EMF on the *q*-axis [12–13].

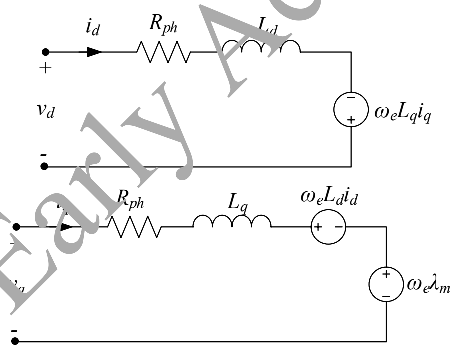

Fig. 1. Equivalent circuit of a permanent magnet synchronous machine in the *d-q* rotating reference frame (generator convention, zero-sequence current neglected)

The electromagnetic torque of a PMSM in the *d-q* coordinate frame is calculated by the formula:

$$T = \tfrac{3P}{4}\left(\psi_d i_q - \psi_q i_d\right), \tag{6}$$

where P is the total number of poles ($P = 2p$, with p the number of pole pairs, for the machine in this study, $p = 10$, $P = 20$). Equations (6) and (7) follow the generator convention, where positive T represents the electromagnetic torque resisting the mechanical input. Substituting the flux linkage expressions $\psi_d = L_d i_d + \psi_f$ and $\psi_q = L_q i_q$ from Eq. (4) into Eq. (6) and expanding yields Eq. (7).

This paper has been accepted for publication in the AEE journal. This is the version, which has not been fully edited and content may change prior to final publication.
Citation information: DOI 10.24425/aee.2026.3546

$$T = \frac{3P}{4}\left[\psi_f i_q + \left(L_d - L_q\right) i_d i_q\right]. \tag{7}$$

The first term, $\frac{3P}{4}\psi_f i_q$ is the magnet torque (proportional to the q-axis current). The second term, $\frac{3P}{4}\left(L_d - L_q\right) i_d i_q$ is the reluctance torque, which exists only when $L_d \neq L_q$ and both current components are nonzero. The factor $(3P/4)$ in Eqs. (6) and (7) follows from the amplitude-invariant Park transformation with P total poles, the equivalent form using pole pairs p is $T = (3p/2)(\psi_d i_q - \psi_q i_d)$. For a surface-mounted AFPM machine (SPM) with symmetric structure, $L_d \approx L_q$, so the reluctance torque is nearly zero. Therefore, to achieve maximum torque, $i_d = 0$ is typically set (all current producing torque through the q-axis component).

2.2. Magnetic saturation in AFPM machines and its effect on L_d, L_q

At low current levels, the magnetic circuit operates linearly, so L_d and L_q are nearly constant. As current increases, the stator teeth and yoke may saturate at approximately 1.5 to 1.7 T, causing the reluctance of the main magnetic circuit to increase along both d and q axes, so both L_d and L_q decrease [10, 15]. This saturation threshold of 1.5–1.7 T is consistent with the B-H curve of the steel_1010 material used for the stator and rotor core in this study, as defined in the Ansys Maxwell material library [11]. For an SPM machine, since the surface magnet has permeability approximately equal to that of air, the d-axis has inherently higher reluctance and typically saturates more strongly, so L_d decreases faster than L_q and the ratio L_d/L_q tends to slightly decrease under deep saturation . This behavior has been reported in surface-mounted PM machines where the d-axis flux path, passing through the magnet and air gap, is more susceptible to iron saturation than the q-axis flux path [12].

Saturation also induces cross-coupling between the two axes. When i_d is large [13, 9], the permanent magnet flux may weaken as the operating point shifts along the demagnetization curve, while the air-gap flux distribution changes and indirectly affects the flux linkage on the q-axis. Conversely, a large i_q may saturate the tooth-tip region and slightly reduce L_d. In this paper, for simplicity, cross-axis coupling is considered small, confirmed by the simulation results in Section 3.1, where the cross-coupling flux change is less than 2% of the main axis flux linkage at rated current and only $L_d(i_d)$ at $i_q = 0$ and $L_q(i_q)$ at $i_d = 0$ are examined.

$$\begin{aligned} \psi_d &= L_d\left(i_d, i_q\right) i_d + \psi_f\left(i_d, i_q\right), \\ \psi_q &= L_q\left(i_d, i_q\right) i_q + \psi_f\left(i_d, i_q\right). \end{aligned} \tag{8}$$

It is important to distinguish between the apparent inductance $L_{\text{app}} = \psi / i$ and the incremental inductance $L_{\text{inc}} = \psi/di$.

The distinction between these inductance types is illustrated in Fig. 2 (taken from Ansys Maxwell Documentation), where the chord slope from the origin to the operating point gives L_{app}, and the tangent slope at the operating point gives L_{inc}. In the unsaturated region both quantities are close, but under saturation L_{inc} is typically significantly smaller and more important for control. The incremental inductance is extracted using the frozen permeability method [13].

This paper has been accepted for publication in the AEE journal. This is the version, which has not been fully edited and content may change prior to final publication.
Citation information: DOI 10.24425/aee.2026.3546

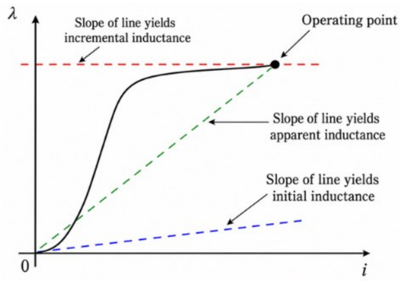

Fig. 2. Nonlinear inductance current and flux linkage

First, a DC operating-point simulation is performed to establish the saturation state. Then the permeability distribution on the finite element mesh is fixed. Finally, a small current perturbation Δi is applied to compute $\Delta\psi$ and derive $L_{\mathrm{inc}} = \Delta\psi/\Delta i$ [7, 13].

2.3. Extracting L_d, L_q from FEM: Method A (*dq* flux linkage) and Method B (phase inductance matrix)

To improve the reliability of the *d* and *q*-axis inductance results, this study performs cross-validation between two methods for deriving L_d, L_q from the same FEM simulation dataset (Ansys Maxwell). The two post-processing approaches are described as follows.

2.3.1. Method A: Based on *dq* flux linkage

At an operating point (i_d, i_q) with a fixed rotor angle, Maxwell can export λ_d, λ_q directly, or they can be computed from λ_{abc} via the Park transformation. For a PMSM model of the SPM type, one can write:

$$\lambda_d = L_d i_d + \psi_f, \tag{9a}$$

$$\lambda_q = L_q i_q, \tag{9b}$$

where ψ_f is the *d*-axis permanent magnet flux linkage component. Then, one gets

$$L_d^{(\mathrm{A})} = \frac{\lambda_d - \psi_f}{i_d}, \tag{10a}$$

$$L_q^{(\mathrm{A})} = \frac{\lambda_q}{i_q}. \tag{10b}$$

These expressions apply when $i_d \neq 0$ and $i_q \neq 0$. For the incremental interpretation, the ratios can be replaced by the local partial derivatives $\partial\lambda_d/\partial i_d$ and $\partial\lambda_q/\partial i_q$ at the operating point. Note that Eq. (10) yields the apparent (chord-slope) inductance $L_{app} = \psi/i$, which equals the incremental inductance only in the linear unsaturated region. For saturated conditions, the incremental form (partial derivatives) should be used. Furthermore, Eq. (10) becomes numerically unstable as i_d or i_q approaches zero and should not be applied in that region.

This paper has been accepted for publication in the AEE journal. This is the version, which has not been fully edited and content may change prior to final publication.
Citation information: DOI 10.24425/aee.2026.3546

2.3.2. Method B: based on the phase inductance matrix $\boldsymbol{L_{abc}}$

From the phase model, one has:

$$\lambda_{abc} = \boldsymbol{L}_{abc} i_{abc} + \psi_{f,abc}\psi_{M,abc}, \tag{11}$$

Where $\boldsymbol{L}_{abc}$ is the inductance matrix obtained from the inductance matrix function or from a magnetostatic analysis at the same saturation condition. Assuming balanced and symmetric three-phase conditions. The full 3 × 3 matrix takes the form:

$$L_{abc} = \begin{bmatrix} L_{aa} & L_{ab} & L_{ac} \\ L_{ba} & L_{bb} & L_{bc} \\ L_{ca} & L_{cb} & L_{cc} \end{bmatrix}, \tag{12}$$

where L_{aa}, L_{bb}, L_{cc} are the self-inductances of phases A, B, C, respectively; L_{ab}, L_{bc}, L_{ca} are the mutual inductances between phases. All elements vary periodically with the rotor position θ.

Assuming balanced and symmetric three-phase conditions:

$$\begin{gathered} L_{aa} = L_{bb} = L_{cc} = L_s \\ L_{ab} = L_{bc} = L_{ca} = M_s \end{gathered}. \tag{13}$$

When exciting with pure d-axis currents $i_a = i_d$, $i_b = i_c = -i_d/2$, and applying the amplitude-invariant Park transformation with the d-axis aligned with phase a at $\theta = 0$, we get the following:

$$\begin{bmatrix} \lambda_d \\ \lambda_q \\ \lambda_0 \end{bmatrix} = \frac{2}{3} \begin{bmatrix} 1 & -\frac{1}{2} & -\frac{1}{2} \\ 0 & \frac{\sqrt{3}}{2} & -\frac{\sqrt{3}}{2} \\ \frac{1}{2} & \frac{1}{2} & \frac{1}{2} \end{bmatrix} \begin{bmatrix} \lambda_a \\ \lambda_b \\ \lambda_c \end{bmatrix}. \tag{14}$$

The d-axis row directly gives:

$$\lambda_d = \frac{2}{3}\left(\lambda_a - \frac{1}{2}\lambda_b - \frac{1}{2}\lambda_c\right). \tag{15}$$

Therefore, one has:

$$L_d^{(B)} = L_s - M_s. \tag{16}$$

Equation (16) is valid under the pure d-axis excitation condition ($i_a = i_d$, $i_b = i_c = -i_d/2$) applied in this study, which ensures that the q-axis flux linkage is zero and the d-axis flux linkage is determined solely by the d-axis current. Similarly, when exciting with pure q-axis current, the result for is also a combination of elements of L_{abc}. Note that the symmetry assumption in Eq. (13) applies only to an ideal machine. In practice, slight geometric asymmetry or slot-harmonic effects may introduce deviations of a few percent, which is reflected in the 7-8% discrepancy observed between Method A and Method B in Section 3. In the general case where absolute symmetry is not imposed, one can directly use the corresponding combinations of L_{abc} to derive L_d and L_q at each operating point.

This paper has been accepted for publication in the AEE journal. This is the version, which has not been fully edited and content may change prior to final publication.
Citation information: DOI 10.24425/aee.2026.3546

2.3.3. Comparison criteria and significance

At each operating point, L_d and L_q are calculated by both methods and compared using the relative deviation. Method A is taken as the reference in Eq. (17) because it directly uses the FEM-computed *dq* flux linkages without additional symmetry assumptions, and thus more faithfully reflects the actual field distribution. The deviation values ε_d and ε_q are signed relative deviations; a deviation within ±10% is considered acceptable for control parameter estimation.

$$\varepsilon_d = \frac{\left|L_d^{(\mathrm{A})} - L_d^{(\mathrm{B})}\right|}{L_d^{(\mathrm{A})}}, \quad \varepsilon_q = \frac{\left|L_q^{(\mathrm{A})} - L_q^{(\mathrm{B})}\right|}{L_q^{(\mathrm{A})}}. \tag{17}$$

Good agreement between the two results indicates that the separation of λ_M, the choice of abc→*dq* transformation, and the saturation conditions in the FEM are consistent. This cross-validation reduces dependence on a single post-processing path and increases the credibility of the reported $L_d(i_d)$ and $L_q(i_q)$ characteristics.

The cross-comparison is performed after the FEM data extraction, before building the control-oriented (linear or current-dependent) parameter model.

2.4. Procedure for determining L_d-L_q

The studied machine is a 4 kW single-stator, dual-rotor axial-flux PM generator of the TORUS type. The slotted stator carries an 18-slot concentrated three-phase winding (39 turns per coil, six-strand 0.71 mm wire, slot fill factor of approximately 0.40), and two outer rotor disks, each carry 20 surface-mounted NdFeB poles, giving $p = 10$ pole pairs. The stator outer and inner diameters are 207.6 mm and 100.8 mm (mean diameter 154.2 mm, active radial length 53.4 mm), with a per-side air gap of 1.1 mm and a magnet thickness of 6.6 mm. The complete set of geometric dimensions is listed in Table 1, and the overall machine structure together with the corresponding Ansys Maxwell pre-processor model is shown in Fig. 3. These dimensions allow the reported inductance and torque results to be independently reproduced.

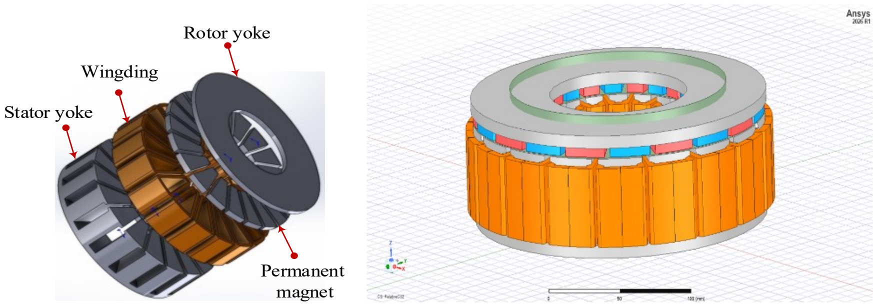

Fig. 3. 3D structure of the AFPMG showing the stator yoke, concentrated winding, rotor yoke and surface-mounted permanent magnets (*left*). Ansys Maxwell 3D pre-processor model (single stator with dual rotor disks) (*right*)

This paper has been accepted for publication in the AEE journal. This is the version, which has not been fully edited and content may change prior to final publication.
Citation information: DOI 10.24425/aee.2026.3546

To determine the $L_d(i)$ and $L_q(i)$ characteristics of the AFPMG, the research team performed 3D electromagnetic simulation using Ansys Maxwell software as illustrated in Fig. 4. The procedure covers from machine geometry construction through to signal extraction and inductance calculation. The main steps are listed as follows:

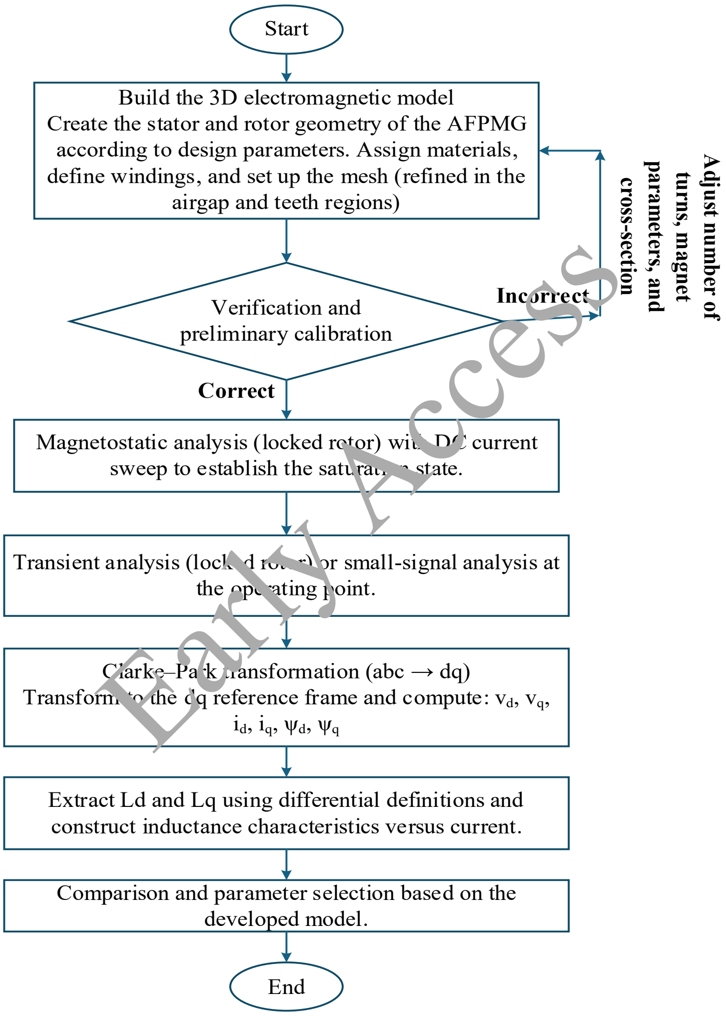

Fig. 4. Simulation and inductance extraction procedure for L_d, L_q of the AFPMG using the 3D finite element method

Step 1. Build the 3D electromagnetic model

Create the stator and rotor geometry according to the design parameters, assign core and magnet materials, and define the three-phase winding. Master-slave periodic boundaries are applied at the two circumferential cut planes of the periodic sector model and a zero-flux

This paper has been accepted for publication in the AEE journal. This is the version, which has not been fully edited and content may change prior to final publication.
Citation information: DOI 10.24425/aee.2026.3546

condition at the outer radial boundary. The mesh is refined at the air gap, tooth-yoke and magnet regions, the 3D model uses approximately 450 000 tetrahedral elements (adaptive refinement) and the 2D model approximately 25 000 triangular elements, with a magnetostatic convergence criterion of $\Delta B/B < 0.1\%$.

Step 2. Preliminary verification and calibration

Run a no-load simulation to verify the induced EMF and the maximum flux density B_{max}, if the EMF requirement or the thresholds of 1.7 T (teeth) and 1.5 T (stator yoke) are not met, adjust the number of turns, magnet dimensions or tooth-yoke cross-sections and repeat. This no-load threshold is intended to avoid excessive global core saturation, not to eliminate saturation entirely: under rated load, local tooth-tip saturation (approximately 1.6–1.7 T, see Section 3) still occurs and is expected, and quantifying its influence on L_d and L_q is precisely the objective of Section 3.

Step 3. Magnetostatic (locked rotor) and DC current sweep to establish saturation

Lock the rotor at positions corresponding to the d and q axes. Perform a DC current sweep from 0 to rated current I_{dm}, in two cases: pure d-axis excitation with $i_q = 0$ and pure q-axis excitation with $i_d = 0$. Record the field distribution and flux linkage to determine the apparent inductance at the operating point, using Eq. (10), as defined in Section 2.3.1

Step 4. Transient (locked rotor) or small-signal analysis at the operating point

Keep the rotor locked and apply a small-amplitude 50 Hz AC current around the operating point of Step 3 along the d- or q-direction, recording the steady-state voltage-current response (RMS values). Since $\omega L >> R$ holds only approximately for this machine ($R = 0.37\ \Omega$, $\omega L \approx 2.2\ \Omega$, an error of approximately 17% if R is neglected), the impedance estimate of Eq. (18) is used only as a supplementary cross-check; the primary results are obtained from Method A, which does not involve this approximation.

$$Z \approx j\omega L\,, \quad L \approx \frac{V_{ph}}{\omega I_{ph}}. \tag{18}$$

Step 5. Coordinate transformation to the dq frame

Transform the signals i, v, ψ from the abc frame to the dq frame using the Clarke-Park transformation at rotor angle θ. Obtain the quantities i_d, i_q, v_d, v_q, ψ_d, ψ_q for axis-by-axis inductance calculation.

Step 6. Extract incremental L_d, L_q and build current-dependent characteristics

Calculate inductance along two parallel paths for cross-validation:

1) Voltage-current path: use $L = X/\omega$ where $X \approx V/I$ under locked-rotor conditions.

2) Flux linkage-current path: compute the incremental inductance using the central finite difference method: $L_d = (\psi_d(i_d + \Delta i) - \psi_d(i_d - \Delta i))/(2\Delta i)$, with $\Delta i = 0.5$ A (second-order accuracy). Similarly for L_q.

$$L_d = \frac{\mathrm{d}\psi_d}{\mathrm{d}i_d}, \quad L_q = \frac{\mathrm{d}\psi_q}{\mathrm{d}i_q}. \tag{19}$$

From this, construct the $L_d(i_d)$ characteristic at $i_q = 0$ and $L_q(i_q)$ at $i_d = 0$, reflecting the saturation effect as a function of operating point.

This paper has been accepted for publication in the AEE journal. This is the version, which has not been fully edited and content may change prior to final publication.
Citation information: DOI 10.24425/aee.2026.3546

Step 7. Cross-validate, select parameters, and integrate into the model

Compare the FEM results across extraction paths using the relative deviations ε_d, ε_q of Eq. (17) and report the maximum deviation. Finally, select L_d, L_q at the rated operating point for the linear model, or build look-up tables $L_d(i)$, $L_q(i)$ for the nonlinear control model.

Table 1. Main parameters of the 4 kW AFPM machine used in simulation

Parameter	**Value**	**Unit**
Rated power P	4.0	kW
Rated phase voltage	128	V(RMS)
Rated phase current	11.21	A(RMS)
Number of pole pairs p	10	
Number of stator slots Q	18	
Magnet material	NdFeB	
Core material	Silicon steel	
Air gap	1.1	mm
Core material	Silicon steel	
B max in teeth	1.5	T
B max in stator yoke	1.3	T
B max in rotor yoke	1.5	T
Inner stator diameter ISD	100.8	mm
Mean diameter D	154.2	
Active radial length L_{stk}	53.4	
Stator yoke thickness d_{sy}	7.4	mm
Slot depth/slot width d_{ss}/w_{ss}	51.9/12.9	mm
Magnet thickness d_m	6.6	mm
Turns per coil	39	
Wire diameter	0.71	mm
Slot fill factor k_{fill}	0.4	

This paper has been accepted for publication in the AEE journal. This is the version, which has not been fully edited and content may change prior to final publication.
Citation information: DOI 10.24425/aee.2026.3546

Figure 5 shows the 3D mesh and distribution of magnetic flux density of the AFPM machine in Maxwell software (half-structure, displaying one rotor disk with magnets and half the stator). Figure 5 (*right*) shows the flux density distribution B in the machine at rated current: the teeth directly beneath the magnets reach approximately 1.6–1.7 T, indicating the iron core is beginning to saturate locally, while the stator yoke region is approximately 1.3 T, consistent with the desired design value.

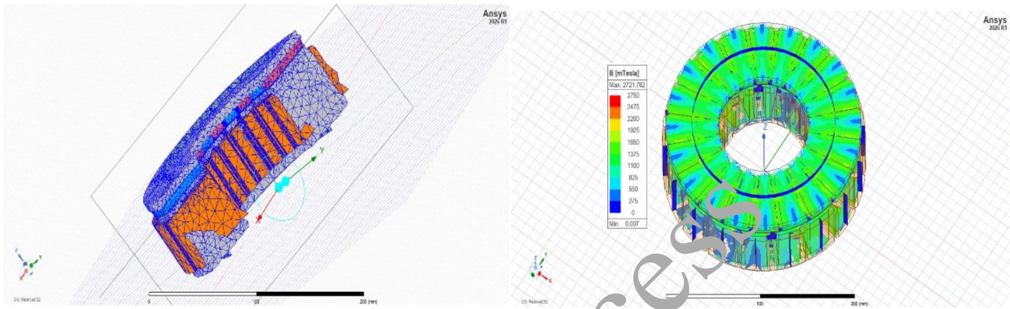

Fig. 5. 3D Mesh of the AFPM generator (*left*) and flux density distribution B at rated current (*right*)

Figure 6 shows the flux density distribution B on the stator and rotor yoke planes, indicating a fairly uniform flux entry into the rotor.

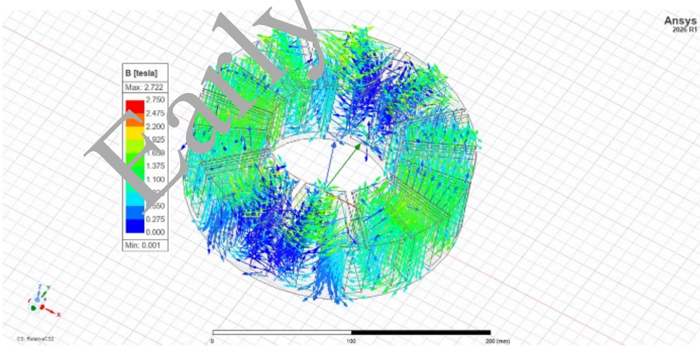

Fig. 6. Flux density distribution B in the stator core of the AFPMG (3D FEM simulation)

3. Results and discussion

3.1. Static 3D simulation results (magnetic-loading)

Figures 7 shows the *d*- and *q*-axis flux linkage characteristics of the generator, respectively. The flux linkage increases proportionally with current up to a certain level and then begins to saturate slightly. From the initial slope of these characteristics (determined by a least-squares linear fit over the linear region, from 0 to 20% of rated current), the initial *d* and *q*-axis inductances are determined to be approximately L_d = 6.8 mH and L_q = 6.4 mH, respectively. L_d

This paper has been accepted for publication in the AEE journal. This is the version, which has not been fully edited and content may change prior to final publication.
Citation information: DOI 10.24425/aee.2026.3546

is slightly higher than L_q, but the difference is relatively small (approximately 6%). This may appear to contradict typical SPM expectations; however, it is attributed to the slot-opening effect: the *d*-axis rotor position places a stator tooth directly opposite the magnet center, while the *q*-axis position aligns a slot opening with the inter-magnet gap, creating slightly higher leakage on the *q*-axis and thus reducing L_q relative to L_d [13].

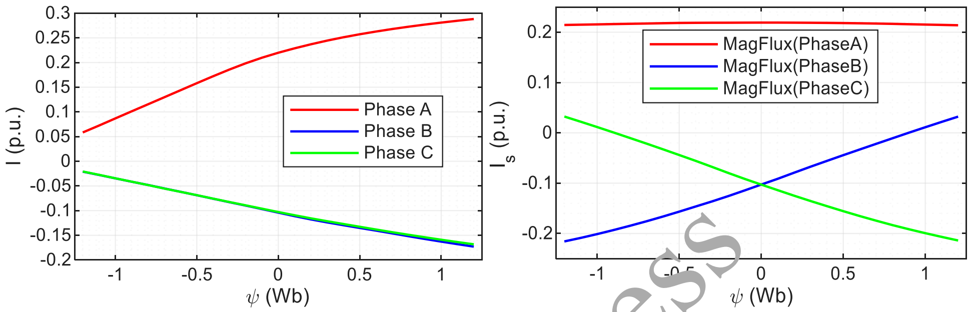

Fig. 7. *d*-axis flux linkage ψ_d (Wb) (*left*) and *q*-axis flux linkage (ψ_q) of the AFPMG as a function of *d*-*q* axis current i_d and i_q (A)

Figures 8 illustrates the flux density distribution B in the stator core of the AFPMG at rated load conditions. It can be seen that the flux density distribution at high-current conditions is concentrated mainly in the iron core region (bright region), reflecting the onset of field saturation.

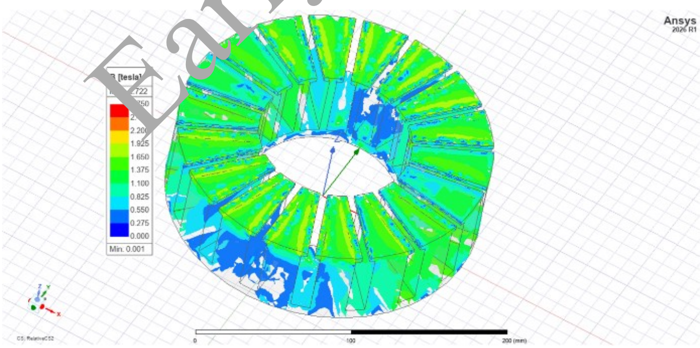

Fig. 8. Flux density distribution B in the stator core of the AFPMG at rated load conditions

Figure 9 shows the variation of L_d and L_q with current; both curves decrease as I_d and I_q increase, confirming that inductance decreases due to core saturation.

This paper has been accepted for publication in the AEE journal. This is the version, which has not been fully edited and content may change prior to final publication.
Citation information: DOI 10.24425/aee.2026.3546

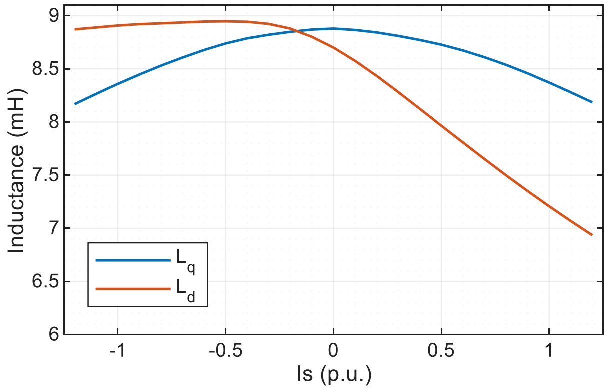

Fig. 9. Variation of L_d and L_q (mH) with armature current I_s (pu), reflecting the effect of magnetic saturation in the iron core

Observation shows that the decrease is not large (the curves are only slightly concave), confirming that the machine has limited magnetic saturation within the normal operating range. This is consistent with the observation in [15] that L_d and L_q depend on current and decrease progressively as current increases.

Thus, the saturation effect causes only a slight reduction in inductance without introducing a significant modeling error. Figures 10 presents the L_q characteristic as a function of the stator current I_s (pu) for two simulation cases: (i) with PM effect and (ii) without PM. The results show that L_q in both cases varies by less than 5% over the full current sweep (relatively flat curve), confirming that the saturation level on the q-axis is small.

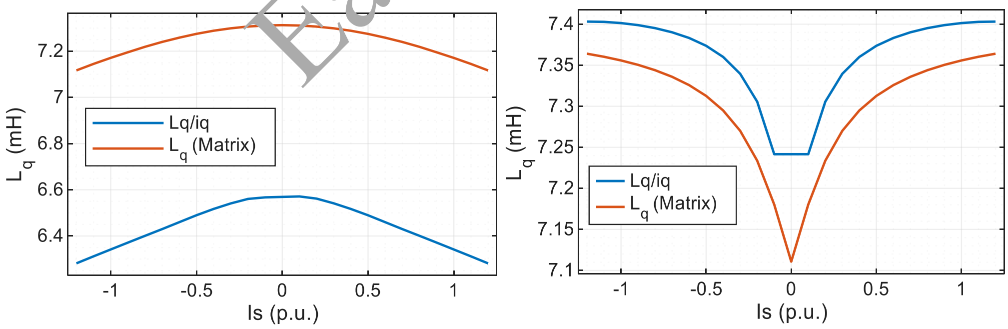

Fig. 10. q-axis inductance (L_q) characteristic with PM effect (*left*) and without PM effect (*right*)

However, when the magnet is included, the resulting L_q is lower than the case without the magnet: around I_s = pu, $L_q \approx 6.34$ mH compared to approximately 7.41 mH. This difference reflects the pre-magnetization effect: the NdFeB magnet establishes a strong DC bias flux in the stator teeth and yoke prior to any armature current, shifting the iron operating point into a region of lower incremental permeability on the B-H curve. This reduces the effective incremental L_q, since the q-axis flux path passes through the stator teeth and yoke where the iron is already partially saturated by the magnet flux. In other words, pre-magnetization changes the effective permeability, altering the incremental L_q-axis inductance. Thus, including the magnet in the model is necessary to obtain L_q close to the actual operating conditions of the machine.

Figure 11 shows the static torque characteristic versus the advance angle (advAngle, defined as the angle between the stator current vector and the q-axis in the dq plane, in electrical degrees) at various stator current magnitudes I_s (pu).

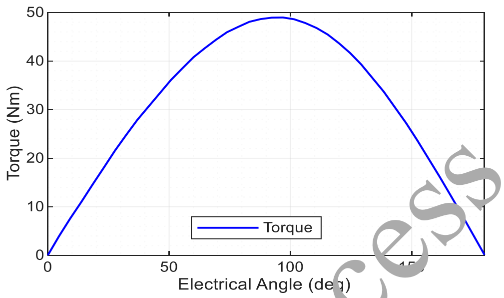

Fig. 11. Static torque T_e (Nm) versus advance angle advAngle (electrical degrees) rated curent I_s (pu) - 3D magnetostatic simulation

Since $L_d \approx L_q$, the reluctance torque component is very small [5], as observed in Fig. 11 where the torque waveform is nearly symmetric. The torque curve obtained from the mathematical model agrees well with the FEM simulation results. The peak error between the model and simulation is only a few percent of the rated value, confirming the accuracy of the control model. Thus, the electromagnetic model based on the determined L_d, L_q can accurately reproduce the actual torque.

3.2. Electromagnetic torque verification via 3D transient simulation

To verify the accuracy of the electromagnetic model and the determined L_d, L_q parameter set, the paper performs a 3D OneEP-Transient simulation (One Electrical Period Transient: an ANSYS Maxwell solver mode that simulates exactly one full electrical cycle under steady-state periodic conditions, providing accurate average torque and ripple values at significantly reduced computation time compared to a full transient startup simulation) with armature current at rated level (I_s = 1 pu). The instantaneous electromagnetic torque T_e is directly compared with the value calculated from the theoretical formula $T_e = 1.5p(\lambda_d\, i_q - \lambda_q\, i_d)$. Figure 12 presents the comparison results [5].

This paper has been accepted for publication in the AEE journal. This is the version, which has not been fully edited and content may change prior to final publication.
Citation information: DOI 10.24425/aee.2026.3546

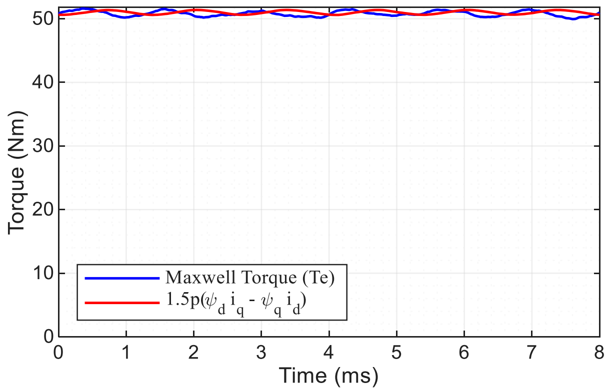

Fig. 12. Comparison of electromagnetic torque T_e (Nm): 3D OneEP-Transient simulation and. analytical formula $T_e = 1.5p(\lambda_d i_q - \lambda_q i_d)$, at rated current ($I_s$ = 1 pu)

From Fig. 12, the instantaneous torque waveform from the transient simulation and the curve calculated from the theoretical formula agree very well throughout the electrical cycle. The average torque from transient simulation is $T_{e,\mathrm{sim}}$ = 50.81 Nm, and from the analytical formula $T_{e,\mathrm{calc}} = 1.5p\ (\psi_d i_q - \psi_q i_d)$ = 50.99 Nm. The deviation is equal to $|50.81 - 50.99|/50.99 \times 100\% = 0.35\%$, confirming the accuracy of the FEM method: 1) the parameter set $L_d \approx 7.04 - 8.37$ mH and $L_q \approx 6.34 - 7.75$ mH determined is consistent with the actual torque characteristics of the machine; 2) the linear *dq* model with these parameters still accurately describes the AFPMG in the normal operating range [5, 12].

3.3. Determination of L_d, L_q via 2D simulation and the effect of the magnet

The 2D model is used not as a substitute for the 3D model but as a computationally inexpensive tool for relative parametric trends; absolute inductance values are taken from the 3D results. To evaluate the effect of including the permanent magnet in the model on the differential inductance value, the paper performs 2D simulation on the unrolled mid-radius cross-section of the AFPM machine (at radius $r_{\mathrm{mid}} = (r_{\mathrm{inner}} + r_{\mathrm{outer}})/2$, transforming the axial-flux geometry into an equivalent linear-motor cross-section) in two cases: with NdFeB N38 magnet and replacing the magnet with vacuum material (vacuum, $\mu_r = 1$, $B_r = 0$). The *q*-axis inductance results from 2D simulation are shown in Figure 10.

Figure 13 shows that L_d from 2D simulation (with NdFeB magnet) decreases slightly from approximately 7.30 mH ($I_s = -1$ pu) to 7.04 mH at rated current - a small saturation level on the *d*-axis. Comparing Fig. 11 with Fig. 12 (without magnet): L_q decreases from ~7.38 mH to ~6.34 mH (–14%) when the magnet is present, due to magnet pre-magnetization increasing local saturation and reducing effective permeability. The results confirm that full magnet modeling is needed to obtain realistic L_d, L_q. For comparison, the 3D static simulation (Method A) yields $L_d \approx 7.04$–8.37 mH and $L_q \approx 6.34$–7.75 mH at rated current, which are 10–20% higher than the 2D results due to end-winding effects and axial leakage flux inherent to the axial-flux geometry but not captured in 2D simulation.

This paper has been accepted for publication in the AEE journal. This is the version, which has not been fully edited and content may change prior to final publication.
Citation information: DOI 10.24425/aee.2026.3546

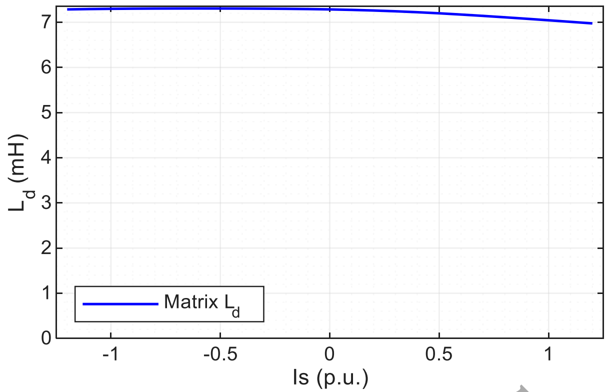

Fig. 13. L_d (mH) from 2D static simulation versus stator current I_s (pu), 2D model with an NdFeB N38 magnet

3.4. Effect of magnet material on L_d and L_q

The magnetization characteristics of the magnet material directly affect the air-gap flux and thus L_d, L_q. The paper compares two materials: NdFeB N38 ($B_r \approx 1.26$ T, $H_c \approx 100.3$ kA/m) and ferrite Y30 ($B_r \approx 0.395$ T, $H_c \approx 195.4$ kA/m). The B-H curves of both materials are presented in Fig. 14 [12].

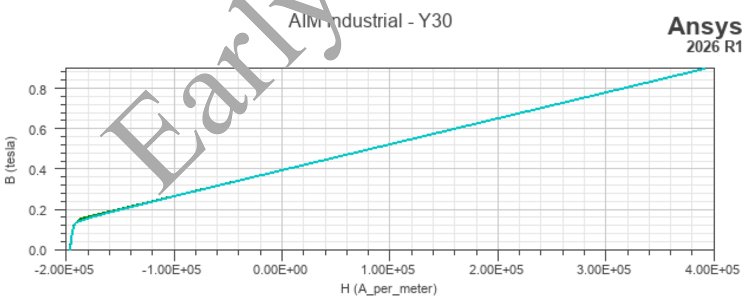

(a)

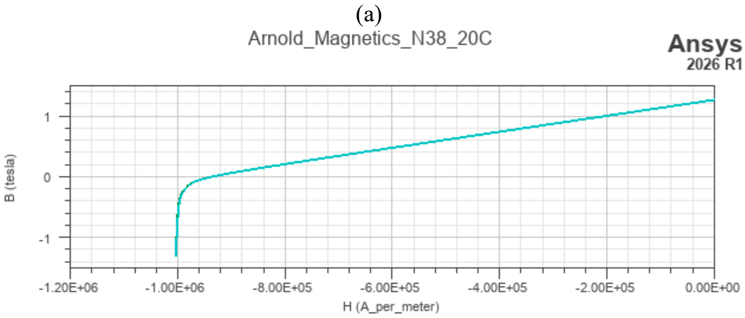

(b)

Fig. 14. B-H curve of ferrite Y30 magnet (a) and NdFeB N38 magnet (b)

This paper has been accepted for publication in the AEE journal. This is the version, which has not been fully edited and content may change prior to final publication.
Citation information: DOI 10.24425/aee.2026.3546

NdFeB N38 has $Br \approx 1.26$ T, approximately three times that of ferrite Y30 ($B_r \approx 0.395$ T). Figure 15 compares the L_d characteristics of the two materials, Fig. 16 compares L_q.

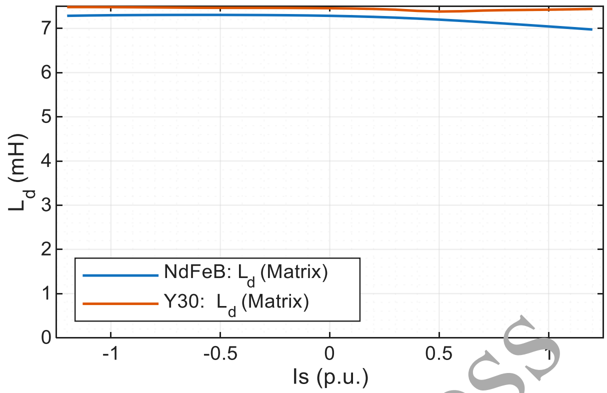

Fig. 15. Comparison of L_d versus I_s(pu) - NdFeB N38 and ferrite Y30 (2D simulation)

From Fig. 15, L_d of NdFeB N38 and ferrite Y30 are nearly identical across the full current range, varying between 7.0–7.3 mH (NdFeB) and 7.0–7.1 mH (Y30); the difference between the two materials is less than 4% across the full current range. This indicates that L_d is primarily determined by the air gap and slot geometry, with little dependence on magnet material type, since both NdFeB and ferrite have relative permeability $\mu_r \approx 1.0$–1.1, approximately equal to that of air. This means the *d*-axis reluctance (which is dominated by the air gap and magnet) is virtually the same for both materials, explaining why L_d is insensitive to magnet material choice when the magnet permeability is close to that of air.

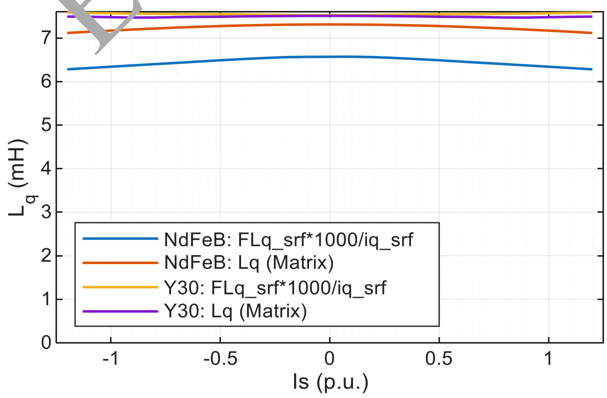

Fig. 16. Comparison of L_q versus I_s(pu) - NdFeB N38 and ferrite Y30 (2D simulation)

From Fig. 16, one can see that L_q of ferrite Y30 (approximately 7.0–7.1 mH) is higher than that of NdFeB (approximately 6.1–6.2 mH), showing a difference of approximately 14–16% at rated current (I_s = 1 pu). This is because NdFeB has higher flux density, pre-magnetizing the iron core more strongly, which reduces the effective permeability on the q-axis and thus pulls L_q lower compared to ferrite Y30. Therefore, magnet material selection primarily affects L_q rather than L_d - an important consideration when building FOC control models for AFPM machines using ferrite magnets. From a control design perspective, the 14–16% difference in L_q between NdFeB and ferrite directly affects the q-axis time constant $\tau_q = L_q/R$ and the MTPA current angle; FOC controllers designed for NdFeB machines should not be directly applied to ferrite variants without re-tuning the L_q parameter. It should also be noted that both B_r and H_c of permanent magnets decrease with temperature (approximately –0.1%/°C for NdFeB Br); the present study uses room-temperature B-H curves, and temperature effects on L_d, L_q are left for future work.

3.5. Effect of air-gap length on L_d and L_q

To isolate the effect of air-gap length, the paper performs a 2D simulation with a fixed NdFeB N38 magnet while varying g from 1 mm to 3 mm (in 0.5 mm steps). The results are shown in Fig. 17.

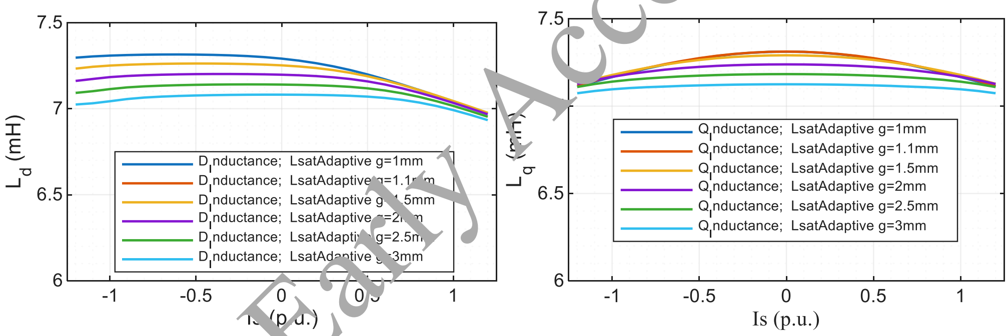

Fig. 17. L_d and L_q characteristic versus I_s (pu) for air gap g = 1–3 mm

Figure 17 shows the characteristic of L_d and L_q inductances with the air gap g = 1–3 mm. Figure 17 (*left*) depicts, as g increases from 1 mm to 3 mm, and L_d decreases from 7.30 mH to 7.02 mH at rated current (I_s = 1 pu), corresponding to a reduction of approximately 3.8%. This is because as the air gap increases, the air-gap reluctance R_{gap} increases accordingly, reducing the total magnetic conductance on the d-axis. In addition, the L_d characteristic at small g (g = 1 mm) tends to saturate more clearly in the region $I_s > 0$ due to higher flux density in the iron core, leading to faster L_d drop under overload [10]. In Fig. 17 (*righ*), the L_q characteristic as a function of current is flatter than L_d, reflecting lower saturation level on the q-axis. L_q decreases from 7.35 mH (g = 1 mm) to 7.10 mH (g = 3 mm), a reduction of 3.4%, smaller than the L_d decrease. This is consistent with the SPM machine characteristic: the q-axis flux path mainly passes through the air gap and magnet material (permeability ≈ air), thus being less sensitive to air-gap variation [10].

Both L_d and L_q decrease as g increases following the same trend, since the air-gap reluctance R_{gap} is dominant. L_d is more sensitive than L_q because the d-axis is directly related to the main

This paper has been accepted for publication in the AEE journal. This is the version, which has not been fully edited and content may change prior to final publication.
Citation information: DOI 10.24425/aee.2026.3546

flux through the magnet. From a design perspective, increasing g helps reduce the axial force in AFPM machines but leads to reduced inductance and torque generation capability a trade-off that must be balanced according to the specific application requirements.

3.6. Comparison of two methods for determining L_d, L_q from 3D simulation

Methods A (based on *dq* flux linkage - see flux data in Fig. 7) and B (based on the L_{abc} inductance matrix) are applied in parallel to the same 3D simulation dataset (magnetic-loading). Figures 18 through 20 present the inductance comparison results from the two methods.

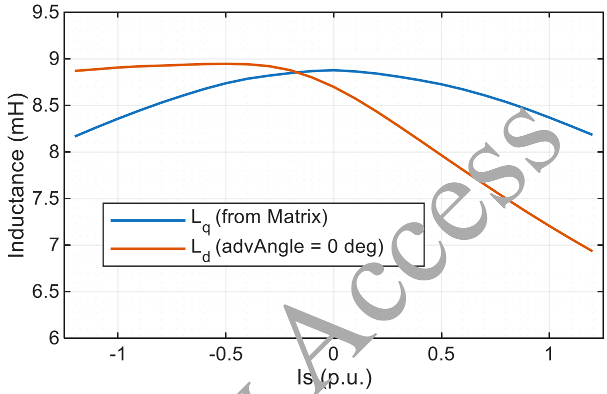

Fig. 18. Comparison of L_d, L_q versus I_s (pu) from 3D simulation: Method B (L_{abc} matrix) and Method A (*dq* flux linkage, advAngle = 0°)

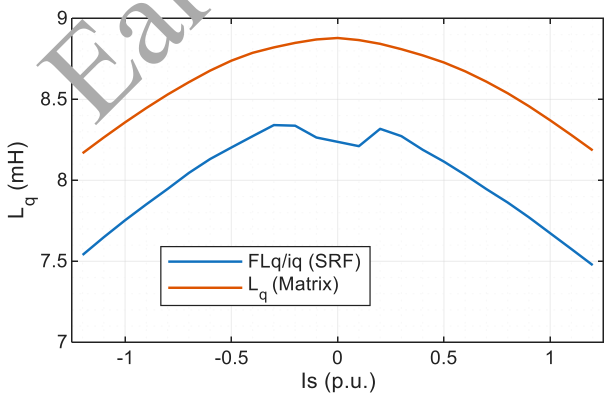

Fig. 19. L_q (mH) versus I_s (pu) from 3D static simulation: comparison of Method A (*dq* flux linkage) and Method B (L_{abc} matrix) at rated excitation angle

From Fig. 18, one can see that L_q (Method B) varies by less than 0.12% over the full current range (8.36 to 8.37 mH), confirming low *q*-axis saturation. L_d varies more clearly and depends on the excitation angle (advAngle): at $I_s = 1$ pu, $L_d(0°) \approx 7.21$ mH while $L_d(90°) \approx 8.37$ mH, a

This paper has been accepted for publication in the AEE journal. This is the version, which has not been fully edited and content may change prior to final publication.
Citation information: DOI 10.24425/aee.2026.3546

difference of ~16%. This phenomenon has the following physical explanation: when current is injected at advAngle = 0° (pure *d*-axis), the flux concentrates in stator teeth directly under the magnet poles, saturating them more strongly and reducing the incremental permeability, hence lowering L_d; at advAngle = 90° (pure *q*-axis), the flux path shifts to the inter-pole region where the iron is less saturated, yielding a higher effective L_d. This direction-dependence of incremental inductance is characteristic of machines with spatially asymmetric local saturation and is the reason that the *dq* flux linkage method (A) should be preferred over the L_{abc} matrix method (B) when high accuracy is required [12].

Figure 19 clearly shows a systematic deviation of approximately 7–8% between Methods A and B when determining L_q from 3D simulation. Method B (L_{abc} matrix) gives higher values (~8.36 mH) because it uses an approximate formula assuming perfect machine symmetry, while Method A (direct *dq* flux linkage) gives ~7.67–7.75 mH, more faithfully reflecting the actual field characteristics. The systematic 7-8% deviation originates from two sources: 1) the perfect symmetry assumption in Method B ignores slot-harmonic-induced inductance variation with rotor position, causing it to overestimate L_q; 2) the difference between chord-slope (apparent) inductance from Method B and tangent-slope (incremental) inductance from Method A becomes non-negligible when the machine operates in the mildly saturated region. Method A is therefore recommended as the primary extraction method for control parameter estimation, as it avoids both sources of error. Both curves are nearly flat with I_s, confirming low *q*-axis saturation in the investigated current range [12].

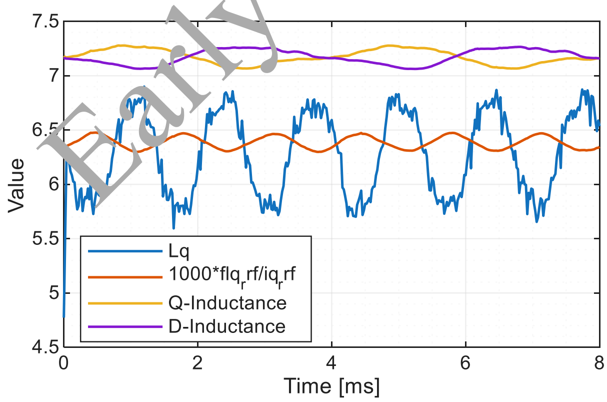

Fig. 20. L_q (mH) from 3D OneEP-Transient simulation compared with Method A and Method B results at rated operating conditions

Figure 20 compares L_q from three calculation methods: OneEP transient simulation (6.28 mH), *dq* flux linkage (6.39 mH), and static magnetic-loading (7.17 mH). The transient simulation value is approximately 12% lower than Magnetic-Loading because transient simulation integrates spatial harmonic effects, end-winding leakage flux, and high-frequency inductance components all neglected in the magnetostatic analysis. This is why the

This paper has been accepted for publication in the AEE journal. This is the version, which has not been fully edited and content may change prior to final publication.
Citation information: DOI 10.24425/aee.2026.3546

experimentally measured L_q (SSFR) typically falls closer to the transient value than to the Magnetic-Loading value [12, 16].

Table 2 summarizes the L_d and L_q inductance results from different methods and simulation modes at the rated operating point (I_s = 1 pu).

Table 2. Summary of L_d and L_q (mH) results from all simulation methods at rated operating point (I_s = 1 pu), with deviation between Methods A and B

Method	**Mode**	**L_d (mH)**	**L_q (mH)**	**L_d-L_q Deviation (%)**
Method A - *dq* flux linkage	3D	7.21 - 8.37	7.67	5–10%
Method B - $\boldsymbol{L}_{abc}$ matrix	3D	8.37	8.37	~0%
Method A - *dq* flux linkage	2D (with NdFeB magnet)	7.04	6.34	10%
Method B - $\boldsymbol{L}_{abc}$ matrix	2D (with NdFeB magnet	8.37	8.37	~0%
Transient simulation	3D (One-EP Transi-ent)	7.17	6.28	12%

Methods A and B yield consistent results (deviation approximately 7–8%). Method A is recommended when high accuracy is required. 3D results are approximately 10–20% higher than 2D due to end-winding effects and axial leakage flux. The transient simulation value ($L_q \approx 6.28$ mH) is closest to the actual value, suitable for FOC control model calibration [5, 10, 12]. The variation in L_d values reported across sections reflects different simulation conditions and methods: 1) $L_d \approx 6.8$ mH is the initial-slope value from the 3D static ψ-i curve at low current (linear region); 2) $L_d \approx 7.04$–7.21 mH is the apparent inductance at rated current from Method A; 3) $L_d \approx 8.37$ mH is from Method B, which overestimates due to the perfect symmetry assumption. These differences are consistent with the theoretical distinction between initial, apparent, and incremental inductance.

4. Conclusion

This paper has established a procedure for determining the *dq*-axis inductances (L_d, L_q) of a 4 kW axial-flux permanent magnet synchronous generator (AFPMG) using 3D FEM simulation combined with theoretical analysis. The main results obtained are as follows. At rated current, $L_d \approx 6.8$ mH and $L_q \approx 6.4$ mH (a difference of approximately 6–7%), showing that this SPM machine has virtually no significant reluctance torque, with the discrepancy mainly due to slot effects and the flux path through the magnets.

Magnetic saturation reduces L_d and L_q by approximately 3–5% over the rated current range, with L_d showing faster reduction than L_q due to stronger saturation of the *d*-axis flux path. The

This paper has been accepted for publication in the AEE journal. This is the version, which has not been fully edited and content may change prior to final publication.
Citation information: DOI 10.24425/aee.2026.3546

d-axis experiences stronger saturation, so L_d decreases faster than L_q, causing the L_d/L_q ratio to slightly decrease under overload.

The 3D FEM procedure with the "frozen permeability" technique and post-processing enables reliable extraction of incremental inductances, with results consistent with analytical methods to within a small error (below 3%). With $L_d \approx L_q$ [6, 9], the assumption of equal inductances still satisfies conventional control requirements [3, 5, 12]; however, in overload regions or sensorless observer algorithms, separate L_d, L_q [3, 15] or nonlinear ψ-i models should be used to improve accuracy. The cross-validation between Method A (*dq* flux linkage) and Method B (L_{abc} matrix) shows a consistent deviation of 7–8%, with Method A recommended for higher accuracy as it directly uses FEM-computed *dq* flux linkages without additional symmetry assumptions.

The present study is limited to simulation-based validation. Physical prototype testing using standstill frequency response (SSFR) experiments is planned as future work to provide experimental confirmation of the obtained L_d, L_q values, while also investigating the effect of temperature on magnet characteristics and the B-H curve to complete the model under actual operating conditions [4, 11].

Acknowledgment

This research is funded by the Vietnamese Government's Project 89.

References

[1] Thongam J.S., Bouchard P., Beguenane R., Okou A.F., Merabet A., *Control of variable speed wind energy conversion system using a wind speed sensorless optimum speed MPPT control method*, IECON 2011-37th Annual Conference of the IEEE Industrial Electronics Society, pp. 855–860 (2011), DOI: 10.1109/IECON.2011.6119422.

[2] Hao Z., Ma Y., Wang P., Luo G., Chen Y., A *Review of Axial-Flux Permanent-Magnet Motors: Topological Structures, Design, Optimization and Control Techniques*, Machines, vol. 10, no. 12 1178 (2022), DOI: 10.3390/machines10121178.

[3] Gadiyar N., Van Verdeghem J., Severson E.L., *Recent advances in analysis and design of axial flux permanent magnet electric machines*, 2021 IEEE Energy Conversion Congress and Exposition (ECCE), pp. 3745–3752 (2021), DOI: 10.1109/ECCE47101.2021.9595085.

[4] Ashrafzadeh S.A., Ghadimi A.A., Jabbari A., Miveh M.R., *Optimal design of a modular axial-flux permanent-magnet synchronous generator for gearless wind turbine applications*, Wind Energy, vol. 27, no. 3, pp. 258–276 (2024), DOI: 10.1002/we.2887.

[5] Xuan H.V., Trong V.N., *Effective Electromagnetic Models for the Design of Axial Flux Permanent Magnet Generators in Wind Power*, Engineering Proceedings, vol. 104, no. 1, 82 (2025), DOI: 10.3390/engproc2025104082.

[6] Duy H.P., Đức Đ.N.,Tiến D.P., *Tính toán điện cảm Ld, Lq cho động cơ IPMSM bằng mạch từ trở tương đương xét đến sự ảnh hưởng của từ thông tản và hiện tượng bão hòa vật liệu từ*, Journal of Measurement, Control, and Automation, vol. 4, no. 3, pp. 39–46 (2023).

[7] Nyitrai A.,Kuczmann M., *Magnetic equivalent circuit and finite element modelling of anisotropic rotor axial flux permanent magnet synchronous motors with fractional slot distributed winding*, IET Electric Power Applications, vol. 17, no. 5, pp. 709–720 (2023), 10.1049/elp2.12298.

This paper has been accepted for publication in the AEE journal. This is the version, which has not been fully edited and content may change prior to final publication.
Citation information: DOI 10.24425/aee.2026.3546

[8] Wang X., Zhang Y., Li N., *Analysis and reduction of electromagnetic noise of yokeless and segmented armature axial flux motor*, In 2022 25th International Conference on Electrical Machines and Systems (ICEMS), pp. 1–6 (2022), DOI: 10.1109/ICEMS56177.2022.9982953.

[9] Song I.S., Jo B.W., Kim K.C., *Analysis of an IPMSM hybrid magnetic equivalent circuit*, Energies, vol. 14, no. 16, 5011 (2021), DOI: 10.3390/en14165011.

[10] Samanta P., Mitikiri S.B., Sahay P.K., Srinivas V.L., *A comparative review of radial and axial Flux PMSMs: Innovations in topology, design, and control*, Franklin Open, 100341 (2025), DOI: 10.1016/j.fraope.2025.100341.

[11] Tsunata R., Izumiya K., Takemoto M., Imai J., Saito T., Ueno T., *Designing and prototyping an axial-flux machine using ferrite PM and round wire for traction applications: Comparison with a radial-flux machine using Nd-Fe-B PM and rectangular wire*, IEEE Transactions on Industry Applications, vol. 60, no. 3, pp. 3934–3949 (2024), DOI: 10.1109/TIA.2024.3371959.

[12] Meessen K.J., Thelin P., Soulard J., Lomonova E.A., *Inductance calculations of permanent-magnet synchronous machines including flux change and self-and cross-saturations*, IEEE Transactions on Magnetics, vol. 44, no. 10, pp. 2324–2331 (2008), DOI: 10.1109/TMAG.2008.2001419.

[13] Sun X., Xiao X., *Precise non-linear flux linkage model for permanent magnet synchronous motors based on current injection and bivariate function approximation*, IET Electric Power Applications, vol. 14, no. 11, pp. 2044–2050 (2020), DOI: 10.1049/iet-epa.2020.0137.

[14] Alsuwian T.M., Habib A., Zainuri M.A.A.M., Ibrahim A.A., Abd Rahim N., Alhawari A.R., Mohamed M.F.P., *Six-Phase Fully Coreless Axial-Flux Permanent-Magnet Generator: Design, Fabrication, and Performance Analysis*, IEEE Access, vol. 13, pp. 22647–22655 (2025), DOI: 10.1109/ACCESS.2025.3526165.

[15] Koothu Kesavan P., Banjerdpongchai D., *Modelling, implementation and analysis of double-side slotted axial flux PMGs suitable to small-scale wind energy conversion systems*, Scientific Reports, vol. 15, no. 1, pp. 1–20 (2025), DOI: 10.1038/s41598-025-08716-6.

[16] Stumberger B., Stumberger G., Dolinar D., Hamler A., Trlep M., *Evaluation of saturation and cross-magnetization effects in interior permanent-magnet synchronous motor*, IEEE Transactions on Industry Applications, vol. 39, no. 5, pp. 1264–1271 (2023), DOI: 10.1109/TIA.2003.816538.